Nano Research 2016, 9(2): 473–489
DOI 10.1007/s12274-015-0929-1
Research Article
ISSN 1998-0124
CN 11-5974/O4

Multifunctional lymph-targeted platform based on Mn@mSiO$_2$ nanocomposites: Combining PFOB for dual-mode imaging and DOX for cancer diagnose and treatment

Tian Liu[1,2,§], Guangyu Wu[3,§], Jiejun Cheng[3], Qing Lu[3], Yanjie Yao[1,2], Zhenjing Liu[1], Dongchen Zhu[1], Juan Zhou[2], Jianrong Xu[3] (✉), Jun Zhu[2] (✉), and Dannong He[1] (✉)

[1] *Country School of Materials Science and Engineering, Shanghai Jiao Tong University, 800 Dongchuan Road, Shanghai 200240, China*
[2] *National Engineering Research Center for Nanotechnology, 28 East Jiang Chuan Road, Shanghai 200241, China*
[3] *Department of Radiology, Shanghai Renji Hospital, Shanghai Jiao Tong University School of Medicine, 1630 Dong Fang Rd, Shanghai 200127, China*
[§] *These authors contributed equally to this work.*

Received: 10 August 2015
Revised: 12 October 2015
Accepted: 27 October 2015

KEYWORDS
multifunctional platform, dual-mode imaging, magnetic resonance imaging (MRI), ultrasound imaging, cancer diagnosis

ABSTRACT

A universal platform with Mn doping and hyaluronic acid (HA) modification, based on mesoporous silica (mSiO$_2$), was designed and used as a basic multifunctional material with magnetic resonance (MR) imaging. Furthermore, we added flexible functions through the addition of functional molecules. Specially, two typical compounds, hydrophobic perfluorooctyl bromide (PFOB) and hydrophilic doxorubicin (DOX), were loaded into the channels to obtain PFOB@Mn@mSiO$_2$@HA (PMMH) or DOX@Mn@mSiO$_2$@HA (DMMH) nanoparticles for dual-mode imaging or imaging and therapy, respectively. The PMMH and DMMH nanoparticles were highly targeted to the lymph system *in vitro* and *in vivo*. MR and ultrasound imaging of PMMH nanoparticles were performed in the lymph system, while MR imaging and chemotherapy of DMMH nanoparticles was used to detect cancer. These results showed that both PMMH and DMMH nanoparticles can be designed with high lymph targeting efficiency. PMMH nanoparticles are a dual-mode contrast agent for both ultrasound and MR imaging for the lymph system and DMMH nanoparticles are powerful agents for the combined diagnosis and therapy of cancer *in vivo*.

1 Introduction

Rapid developments in nanotechnology have enabled the development of various functional nanomaterials with multiple discrete function-related components integrated into one nanoparticle. These have allowed

Address correspondence to Dannong He, hdn_nercn@163.com; Jun Zhu, yzjzhu@163.com; Jianrong Xu, renjixujr@163.com

for applications in biomedical imaging and therapy to overcome limitations related to nanoparticles with single functions [1, 2]. These multifunctional nanomaterials can be used in the biomedical sciences in areas such as diagnosis, drug delivery, hyperthermia, stem cell therapy, and tissue engineering. Therefore, it is interesting to design a multifunctional nanoprobe for combined imaging, because each imaging modality has its own limitations and advantages. For instance, numerous nanoprobes used in luminescent imaging [3–5], computed tomography (CT), and magnetic resonance (MR) imaging (MRI) [6–8] have been applied for cancer diagnosis to improve sensitivity and accuracy [3–8]. Additionally, it is also meaningful to develop a multifunctional nanoarchitecture for combined therapy or diagnosis and therapy by encapsulating functional materials within a designed nanoparticle system. For example, combined chemotherapy and imaging or photothermal therapies and chemotherapies has been reported previously [3, 9–12]. However, despite the extensive applications of these multifunctional nanoarchitectures, their functions are restricted once the architectures are fabricated. Therefore, it is difficult to add or change the functions of these multifunctional nanoarchitectures. The development of a more universal platform is necessary, which can be conveniently endowed with varies properties by different post-processing methods after synthesis per the specific diagnostic and therapeutic demands.

To make this design feasible, a basic material with a sophisticated structure and fundamental function is needed. Mesoporous silica ($mSiO_2$) has attracted considerable attention in recent years because of its advantageous structural properties such as high internal surface area, pore volume, tunable pore sizes, colloidal stability, and the possibility to specifically functionalize the inner pore system or the external particle surface. These highly attractive features make $mSiO_2$ a promising and widely applicable platform for diverse biomedical applications including in bioimaging, biosensing, biocatalysis, bone repair, and scaffold engineering, and drug delivery. Numerous recent studies have attempted to create multifunctional nanoparticles comprising $mSiO_2$ as the host material, such as the multistage delivery system and multimodal imaging system. Specially, some metal ions for magnetic resonance imaging, such as Mn^{2+} and Gd^{3+}, have been doped into the framework of $mSiO_2$, which contributes to the development of a platform that can be used with MR imaging. The platform further absorbed drug molecules to fabricate a multifunctional nanoarchitecture with drug delivery and MR imaging. Thus, a modified $mSiO_2$ may be used as a basic material with a sophisticated structure and fundamental function to produce and change their multifunctional properties conveniently by absorbing different molecules.

Hyaluronic acid (HA) is a well-known natural polysaccharide that is widely distributed in the extracellular matrix. Given its biocompatibility and diverse biological functions as a targeting ligand and signaling molecule, HA has been used as a superior biomaterial in the formulation of nanospheres, hydrogels, and scaffolds for drug delivery and tissue engineering [13]. In addition, because of the interaction between HA and the CD44 receptor, HA is widely used as a tumor vector for targeting procedures CD44 is expressed in a variety of tumors such as breast, colon, intestinal, and brain tumors [14, 15]. Furthermore, lymphatic endothelial hyaluronan receptor-1 (LYVE-1), as a new homolog of the CD44 glycoprotein, is a lymph-specific receptor for HA that can bind both soluble and immobilized HA [16–18]. However, unlike CD44, LYVE-1 can colocalize with HA on the luminal face of the lymph vessel wall and is completely absent from blood vessels. Therefore, HA is highly promising as a lymphatic targeting carrier. In our preliminary report [19], a pure HA molecule was used as a targeted matrix to the lymphatic system. Our results showed that HA was capable of defining the structure of the lymphatic system and was highly targeted to the lymphatic system *in vitro* and *in vivo*.

Here, we designed a universal and multifunctional platform from widely used materials, including $mSiO_2$ as the media, HA as the targeted matrix, and Mn for an MRI element. The platform is inexpensive, practical, and flexible. Based on this platform, we further developed a multifunctional probe for MR and ultrasound imaging to improve the sensitivity and resolution for lymph imaging and a multifunctional vehicle with accurate positioning and chemotherapy for targeting lymph tumors. According to previous reports, some nano-/micro-carriers prepared using perfluorocty

bromide (PFOB) have been utilized as ultrasound contrast agents [20]. Therefore, in the present study, PFOB was loaded into Mn@mSiO$_2$@HA (MMH) nanoparticles to obtain PFOB@Mn@mSiO$_2$@HA (PMMH) nanoparticles, in which PFOB could enhance sound reflection function and further improve the ultrasound contrast signal. Doxorubicin (DOX, a general chemotherapeutic drug) was also loaded onto MMH nanoparticles to obtain DOX@Mn@mSiO$_2$@HA (DMMH) nanoparticles. Thus, two typical compounds, hydrophobic PFOB and hydrophilic DOX, were used as models to obtain PMMH or DMMH nanoparticles for dual-mode imaging as well as imaging and therapy, respectively. We found that the PMMH and DMMH nanoparticles were highly targeted to the lymph system *in vitro* and *in vivo*. We also conducted MR and ultrasound imaging of PMMH nanoparticles in the lymph system and MR imaging and chemotherapy of DMMH nanoparticles in cancer. We also describe the use of our new universal platform for additional applications.

2 Experimental

2.1 Preparation of manganese-doped mesoporous silica (Mn@mSiO$_2$, MM) nanoparticles

MM nanoparticles were synthesized as follows: 1.2 mmol of cetyltrimethyl ammonium bromide was dissolved in 180 mL of double-distilled water at room temperature. Next, 6 mmol of NaOH was added to the solution, followed by 10 mmol of triethoxysilane under rigorous stirring. Subsequently, 0, 0.1, 0.5, 1, and 5 mmol $MnCl_2{\cdot}4H_2O$ were added rapidly. The obtained precipitates were recovered by filtration after 24 h of rigorous stirring, washed, and refluxed in 7.2 mg·mL^{-1} ammonium nitrate ethanol solution to remove the cetyltrimethyl ammonium bromide.

2.2 Preparation of Mn@mSiO$_2$@HA nanoparticles

The preparation of MMH nanoparticles included the surface modification of MM nanoparticles with 3-aminopropyl triethoxysilane and the conjugation of HA. In a typical experiment, 0.1 g of MM nanoparticles was reacted with 110 μL of 3-aminopropyl triethoxysilane in 10 mL toluene. The amino-modified MM nanoparticles were washed with methanol and water, centrifuged, and dried at 60 ℃ for 12 h. Next, HA was activated using N-hydroxysuccinimide and N-ethyl-N′-[3-(dimethylamino)propyl] carbodiimide hydrochloride. Specifically, 1.25 g of HA and the obtained amino-modified MM nanoparticles were dissolved in 200 mL double-distilled water. Subsequently, 0.23 g of N-ethyl-N′-[3-(dimethylamino)propyl] carbodiimide hydrochloride and 0.14 g of N-hydroxysuccinimide were added into the solution and stirred for 24 h at room temperature. Finally, the resulting products were collected by centrifugation, washed with ethanol and water three times, and dried at 60 ℃.

2.3 Preparation of PFOB@Mn@mSiO$_2$@HA and DOX@Mn@mSiO$_2$@HA nanoparticles

First, 0.1 g of MMH nanoparticles was dispersed into 30 mL double-distilled water, and then 500 μL of 2 mg·mL^{-1} DOX or 100 μL of PFOB was injected. After stirring for 24 h, PMMH or DMMH were fabricated and separated. To remove the free PFOB and DOX in the solutions of nanoparticles, PMMH and DMMH were washed with double-distilled water approximately 5 times until the supernatant liquid was clear.

2.4 Characterization

Powder X-ray diffraction (XRD) patterns were recorded on the Rigaku D/MAX-2250V diffractometer (Tokyo, Japan) using Cu-Ka radiation (40 kV and 40 mA). The morphology of the samples was determined using a high-resolution transmission electron microscope (HRTEM, JEOL, JEM-2100F) and a field-emission scanning electron microscope (FESEM, S-4800, Hitachi, Tokyo, Japan), respectively. The Fourier transformation infrared (FT-IR) spectra were recorded on a Nicolet 6700 FT-IR spectrometer (Thermo Fischer, Waltham, MA, USA). The UV–vis spectra were investigated using a PerkinElmer Lambda 950 UV-vis spectrophotometer (Waltham, MA, USA). The Brunauere-Emmette-Teller surface area and pore size were measured using a Micromeritics ASAP 2020 instrument (Norcross, GA, USA). X-ray photoelectron spectroscopy (XPS) was performed using a VG Scientific ESCLAB 220iXL X-ray photoelectron spectrometer (Uppsala, Sweden). The average hydrodynamic sizes were measured using

a Malvern Zetasizer Nano ZS (Malvern Instruments Ltd., Malvern, Worcestershire, UK) based on dynamic light scattering. The contents of Mn were analyzed by inductively coupled plasma optic emission spectrometry (ICP-MS) using a PLASMA-SPEC-II instrument (Horiba Jobin Yvon, Inc., Kyoto, Japan). Fluorine content was determined by high-performance ion chromatography (Dionex 500, Sunnyvale, CA, USA) with conductivity detection through oxygen flask combustion (separating column: IonPac AG14-AS14; eluent: 0.0010 M $NaHCO_3$ + 0.0035 M Na_2CO_3). Based on the results, the loading content of PFOB in PMMH nanoparticles was calculated.

2.5 Cell viability experiments

HCT116 cells (5 × 10^3 cells·well^{-1}) in log phase were incubated into 96-well flat-bottomed plates. The cells were incubated for 24 h at 37 ℃ under 5% CO_2. The obtained PMMH nanoparticles at concentrations of 0, 25, 50, 75, 100, and 125 μg·mL^{-1} in phosphate-buffered saline (PBS) were added to the wells of the treatment group. The cells were incubated for 4, 8, and 12 h at 37 ℃ under 5% CO_2. Next, all nanoparticles were removed from the medium and 10% CCK/PBS solution was added to each well and incubated at 37 ℃ for 4 h. The amount of cell proliferation was measured by reading the optical density value at 450 nm using a plate reader. The following formula was used to calculate cell viability: viability (%) = (mean of absorbance value of treatment group/mean absorbance value of control) × 100%. The results were expressed as an average over five nominally identical measurements.

2.6 Confocal imaging of cells

Confocal imaging of cells was performed using a Leica laser scanning confocal microscope (Wetzlar, Germany). HCT116 cells (1 × 10^6 cells·mL^{-1}) were incubated with fluorescein isothiocyanate (FITC)-labeled nanoparticles (MM, MMH, and PMMH) for 2 h for confocal imaging, fixed with 4% paraformaldehyde for 30 min, and stained by DAPI for 8 min. All cells were washed twice with PBS before confocal imaging. Imaging of FITC-labeled nanoparticles was carried out at 488 nm laser excitation, with emission collected from 550 to 570 nm.

2.7 MRI *in vitro*

All MRI scans were carried out with a 3.0 T whole body system (3.0 T Intera Achieva, Philips Medical Systems, Best, The Netherlands) with a brain crossed coil. Different mass concentrations of PMMH nanoparticles were placed in a series of PE tubes for T_1-weighted MR imaging using a standard spin echo sequence. The sequence parameters were TR/TE, 4.6/2.4 ms; flip angle, 12°; FOV, 26 cm; matrix, 320 × 256; effective slice thickness, 0.6 mm. The 3D MRIs were then reconstructed from the original data set at each time point using maximum-intensity projection.

2.8 Ultrasound imaging *in vitro*

Ultrasound imaging was performed using the Acuson Sequoia 512 linear transducer (Siemens, Mountain View, CA, USA). A dilute solution (1 mg·mL^{-1}) of PMMH nanoparticles was placed in dialysis cassettes and examined using a Siemens Acuson Sequoia 512 with a 3.5 MHz linear transducer.

2.9 MRI *in vivo*

Animal experiments were approved by local governmental authorities. Experiments were carried out on New Zealand White Rabbits with weights of 3–3.5 kg, which were anaesthetized by intraperitoneal injection of 3% pentobarbital solution. During this process, the rabbit body temperature was maintained at a physiological level. PMMH nanoparticles (400 μL, 0.10 mg·mL^{-1}) and gadopentetate (400 μL) were injected into the right and left knee popliteal fossa, respectively. The injection sites for the contrast agents were carefully disinfected. After injection, the injection sites were gently massaged for approximately 30 s to improve lymph drainage. The MR imaging area of interest was from the upper thigh to the shank. Similarly, a nude mouse weighing 28.4 g was anaesthetized and injected in the tumor region with 150 μL DMMH (0.10 mg·mL^{-1}), and MR images were collected using a small animal crossed coil.

All MR imaging was performed on a 3.0-T superconductive whole-body scanner (Signa HDXt GE Healthcare, Little Chalfont, UK), using a dedicated six-channel phased array sensitivity encoding coil for optimized signal reception with the rabbits in the

supine position. The conventional gradient system with an amplitude of 40 $mT \cdot m^{-1}$ and a slew rate of 150 $mT \cdot m^{-1} \cdot ms^{-1}$. For interstitial MRI, a fast T_1-weighted 3D gradient-echo sequence in the coronal plane was acquired after gadopentetate dimeglumine injection. To assess all phases of lymph node enhancement, we began acquiring images immediately after subcutaneous administration of two contrast agent every 10 min. The sequence parameters were TR/TE, 4.6/2.4 ms; flip angle, 12°; FOV, 26 cm; matrix, 320 × 256; effective slice thickness, 0.6 mm. The 3D MRIs were then reconstructed from the original data set using maximum-intensity projection. During the acquisition, the position the rabbit being examined rabbit remained unchanged.

2.10 Ultrasound imaging *in vivo*

Animal experiments were approved by local governmental authorities. Experiments were carried out using New Zealand White Rabbits with weights of 3–3.5 kg, which were anaesthetized by intraperitoneal injection with 3% pentobarbital solution. During the process, the rabbit body temperature was maintained at a physiological level. Furthermore, the skin of leg knee popliteal area was shed using 6% NaS. PMMH nanoparticles (400 μL, 0.10 $mg \cdot mL^{-1}$) were injected into the right knee popliteal fossa, before which primary gray scale sonography was conducted to locate lymph nodes in the leg knee popliteal area. All ultrasound imaging was performed using a High-Resolution *In Vivo* Ultrasound Micro-Imaging System with ECG 2500mv and Resp 2590mv.

2.11 Immunofluorescent antibody staining analysis

Rabbit anti-human LYVE-1 polyclonal primary antibodies were optimized and validated in formalin-fixed paraffin. Tissues in the knee popliteal fossa region, which were imaged successfully by ultrasound and MR imaging, were removed from the rabbit, fixed in PBS containing 4% paraformaldehyde, and embedded in paraffin wax. Prior to staining, the tissues were fixed, dehydrated, wax-impregnated, embedded, and sliced. Primary antibody dilutions (1:50) were incubated with tissue slides for 90 min at room temperature. Lymph vessels from the rabbit leg knee popliteal fossa were used as positive control tissues to validate LYVE-1. The slides were viewed using a Zeiss Axioskop fluorescence microscope with fluorescent illumination.

2.12 DOX loading and *in vitro* drug release

First, 50 mg of MMH nanoparticles was added into 50 mL 1 $mg \cdot mL^{-1}$ DOX aqueous solution. After stirring for 24 h, the DMMH nanoparticles with loaded drugs were fabricated and separated. Next, 5 mg of DMMH nanoparticles was immersed in 10 mL PBS (pH 5.5), which was introduced into dialysis cassettes (width of 44 mm, M_W cut-off is 8,000–14,000) as the drug donor. The bag was placed in 100 mL PBS as the release medium (receiver). The release medium (10 mL) was removed for the determination of UV spectra at approximately 490 nm at given time intervals and replaced with the same volume of fresh buffer solution. The curve showing the release rate for DOX was obtained from the relationship between the cumulative release amount and time t. Additionally, the standard curve of the DOX aqueous solution was obtained from the relationship between the absorbance and the DOX concentration.

2.13 Growth inhibitory effect of DMMH nanoparticles on tumor cells

The growth inhibitory effect of DMMH nanoparticles on HCT116 tumor cells was evaluated in a CCK assay as described previously [21–23]. The cells were seeded into a 96-well plate (5,000 cells in 100 $\mu L \cdot well^{-1}$) and cultured for 24 h. The medium was then substituted with a series of concentrations of free DOX and DMMH nanoparticles. Two days later, the formulations were removed and CCK solution was added and incubated for 4 h. Next, the CCK solution was removed and PBS was added to the wells. The absorption, representing cell viability, was detected using a microplate reader (iMark/xMark Bio-Rad, Hercules, CA, USA) to determine the cell viability at 450 nm.

2.14 Growth inhibition of DMMH nanoparticles on tumors *in vivo*

Male specific pathogen-free nude mice, age 4–5 weeks and weighing 18–20 g were supplied by the Department of Experimental Animals, Shanghai Jiaotong University, and maintained under standard housing conditions.

All animal experiments were carried out in accordance with guidelines evaluated and approved by the ethics committee of Shanghai Jiaotong University.

YAC-1 (mouse lymphoma cells) tumor bearing mice were established by subcutaneous injection of 2×10^6 cells suspended in 200 μL PBS. Three groups of mice ($n = 6$), for a total of 18 mice, were subcutaneously injected with PBS, free DOX, and DMMH nanoparticles (0.1 mg·mL^{-1}) with the same dosage of free DOX inside, respectively, until the diameter of tumor was around 8–10 mm, after which all mice were returned to animal housing. The tumor volumes were tracked every 2 days using vernier calipers. Tumor volumes were calculated using the formula $V = 1/2 (L \times W^2)$, where L and W were the length (longest dimension) and width (shortest dimension). On the 23th day, all animals were euthanized and the tumors were dissected and weighed.

2.15 Tissue distribution

The short-term distribution of MMH nanoparticles in mice was determined as follows: 18 mice were divided into six groups with three mice in each group. Three mice were used as control group. Based on the preliminary experiment, the dosage in this experiment of MMH nanoparticles was 0.1 mL 250 mg·kg^{-1}. Three mice in each group were sacrificed and anatomized at 4, 6, 8, 10, and 12 h after being injected by MMH nanoparticles in the enterocoelia except the control group that had not been injected. Approximately 100 μL of blood sample was obtained in each group. Furthermore, the liver, lung, spleen, brain, heart, and kidney were collected. Organs were weighed and homogenized. After subjecting the sample to a digestion process, the Mn content was determined by ICP-MS.

The long-term distribution of MMH nanoparticles in mice was determined as follows: Nine mice were divided into three groups, with three mice each group, and three mice used as a control group. Based on the preliminary experiment, the dosage in this experiment of MMH nanoparticles was 0.1 mL 250 mg·kg^{-1}. Three mice from each group were sacrificed and anatomized at 1, 2, and 3 days after being injected with MMH nanoparticles in the enterocoelia. The control group received no injections. Beginning on day 1, all three mice in each group were intravenously injected once daily for 3 consecutive days. The injections were tolerated well and no adverse effects were observed during the entire experiment. On days 1, 2, and 3, approximately 100 μL of blood sample was obtained in each group before the liver, lung, spleen, brain, heart, and kidney of the treatment-groups were collected at 12 h after injection. Organs were weighed and homogenized. After subjecting the sample to a digestion process, the Mn content was determined by ICP-MS.

2.16 Statistical analysis

The results are expressed as the mean ± standard deviation (SD). Statistical analysis was conducted using Student's t-test. Differences were considered significant at $P < 0.05$.

3 Results and discussion

MM nanoparticles were obtained by mesoporous silica material doping Mn ions via a co-assembly process, which may be used as basic multifunctional materials for MR imaging. Furthermore, the surface grafting of MM nanoparticles by HA resulted in the development of a multifunctional platform for targeted delivery to specific tumor cells and organisms. In order to evaluate the flexibility of the multifunctional platform, hydrophobic PFOB and hydrophilic DOX molecules were loaded into the platform for dual-mode imaging with MR and ultrasound imaging for the lymph system and combined diagnosis and therapy with MR imaging and sustained release near a lymph tumor. The procedure is schematically illustrated in Fig. 1. Figure S1 in the Electronic Supplementary Material (ESM) shows that the multifunctional platform included 5 mmol Mn ions, which produced a surface area of 503 m^2·g^{-1}. Moreover, the platform was used to absorb hydrophobic PFOB to prepare PMMH nanoparticles for dual-mode imaging, and PFOB loaded in the MMH nanoparticles was determined to be 11.2 mg·g^{-1}.

Similar to the results of Shi et al. [24], the driving force of the hydrophobic PFOB molecule in MMH nanoparticles may have been the hydrophobic interaction

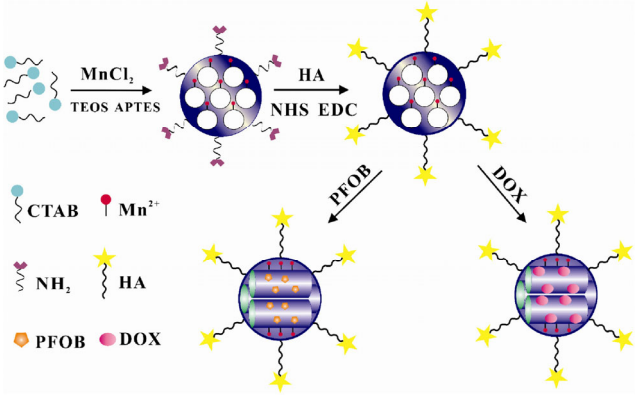

Figure 1 Schematic illustration of the formation of PMMH and DMMH nanoparticles.

between PFOB and the HA molecule in mesoporous pores. The morphology and structure of PMMH nanoparticles were characterized. Scanning electron microscopy (SEM) and transmission electron microscopy (TEM) images of the PMMH nanoparticles are presented in Figs. 2(a) and 2(b), respectively. Figure 2(a) shows that the PMMH nanoparticles were well-dispersed with uniform sizes and an average diameter of approximately 150 nm, which is in accordance with the results for the average hydrodynamic size shown in Fig. S2 (in the ESM). Furthermore, regular hexagonal arrays of uniform pore openings were observed in TEM images of as-synthesized PMMH nanoparticles (Fig. 2(b)). The small-angle XRD patterns revealed the same results. As shown in Fig. 2(c), the main (100) diffraction peak of typical mesoporous silica materials is shown, indicating that mesoporous silica was maintained, although the channel frameworks may have been destroyed by doping with Mn ions. A typical type IV isotherm with a steep capillary condensation step also indicated an excellent quality mesoporous material with a surface area of 374 $m^2 \cdot g^{-1}$ (Fig. 2(d)) and pore size of 3.0 nm (Fig. S3 in the ESM), although the mesoporous pores were filled with PFOB molecules. Moreover, as shown in Fig. S4 (in the ESM), the decrease in surface area may have resulted from HA modification and PFOB absorption, which was further characterized by the FT-IR spectra of PFOB, HA, and PMMH nanoparticles. As shown in Fig. 2(e), the typical peaks of PFOB, such as 1,245 and 1,218 cm^{-1}, were monitored, and these peaks were attributed to characteristic asymmetric stretching vibrations of the $-CF_2$ group [12, 25, 26]. Furthermore, typical peaks of HA, such as 1,610 and 1,040 cm^{-1}, were found, resulting from the characteristic stretching vibrations of C=O and bending vibration of N–H, respectively. Compared to the main characteristic peaks of PFOB and HA, all peaks were found in the FT-IR spectra of the PMMH nanoparticles in addition to 1,150 cm^{-1}, the characteristic stretching vibration of C–N. These results indicate that PFOB and HA were added to MM nanoparticles successfully, which was further supported by XPS results, analysis of the elemental composition, and their chemical environment in PMMH nanoparticles. The desired elements, such as Si, C, N, O, Mn, and F, are encapsulated in PMMH nanoparticles, and the Mn (2p) feature centered at 641.2 eV, which is the typical binding energy of the metal–silicate (Mn–O–Si) [27–29]. Furthermore, EDX revealed that the Mn content was approximately 5.6% in the PMMH nanoparticles. The above results demonstrate the development of a universal platform with Mn doping and HA modification based on $mSiO_2$ with absorbed hydrophobic PFOB for use as a multifunctional platform.

To evaluate the targeting specificity of the PMMH nanoparticles to the lymph system, the cellular uptake efficiency of the PMMH nanoparticles was observed by confocal laser scanning microscopy. Based on previous studies [16, 30–32], receptor-mediated endocytosis, particularly an interaction between HA and the CD44 receptor, was identified as the principal cellular uptake mechanism of HA-based nanoparticles. Furthermore, the amino acid sequence in the extracellular domain of LYVE-1, a lymphatic endothelial-specific marker in the lymph system, and CD44 share 43% homology as homologs [33]. Therefore, some cells showing wide expression of CD44 were used to simulate the interaction between the lymph system and HA-based nanoparticles. Thus, in the present experiment, HCT116 cells were used as high CD44 receptor-expressing cells, while HEK293 cells were regarded as control groups because of their low expression of endogenous ligand receptor [34], and FITC, a near-infrared fluorescence dye, was used to detect the cellular uptake and distribution of the nanoparticles.

As shown in Fig. 3, HCT116 and HEK293 cells with blue fluorescence were dyed with DAPI and green

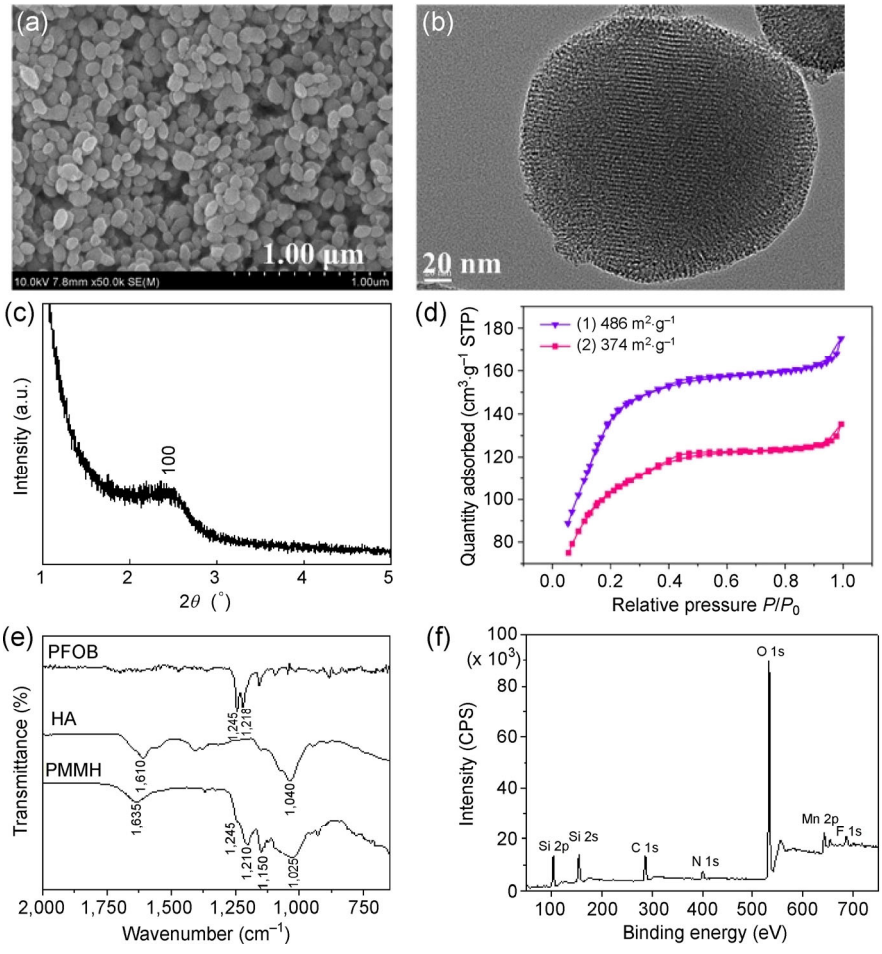

Figure 2 (a) SEM, (b) TEM, and (c) XRD pattern of PMMH nanoparticles, (d) N_2 adsorption/desorption isotherm ((1): MMH nanoparticles and (2): PMMH nanoparticles), (e) FT-IR spectra and (f) XPS spectra of PMMH nanoparticles.

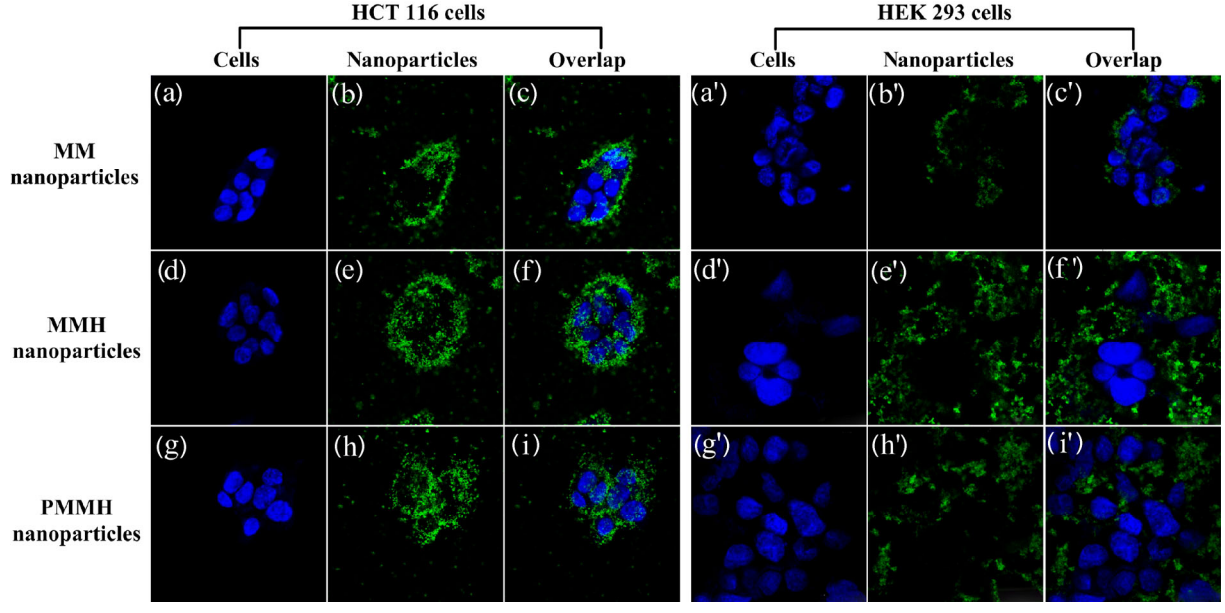

Figure 3 Laser scanning confocal microscopy images of HCT116 and HEK293 cells incubated with MM, MMH, and PMMH nanoparticles. All images were acquired under identical instrumental conditions and presented at the same intensity scale.

FITC-labeled nanoparticles. In HCT116 cells, HA-based MMH nanoparticles embraced the cells largely and were tightly distributed around the cells (Fig. 3(f)), which differs from the results of MM nanoparticles (Fig. 3(c)), which showed general cellular uptake of the nanoparticles. This result revealed that MMH has strong affinity towards HCT116 cells. Furthermore, the addition of PFOB in MMH nanoparticles had little influence on the targeting specificity (Fig. 3(i)). However, in HEK293 cells, all MM, MMH and PMMH nanoparticles showed poor phagocytic activity in the cells (Figs. 3(c′), 3(f′) and 3(i′)). These results indicate that the CD44 receptor was overexpressed, giving the developed HA-based nanoparticles high lymph targeting efficiency.

The MR and ultrasound imaging of the PMMH nanoparticles were conducted to evaluate their multifunctional diagnosis abilities. The MR imaging signals of the PMMH nanoparticles were measured *in vitro*. Different mass concentrations of PMMH nanoparticles in the centrifuge tubes, as well as pure water for the background signal, were measured to determine the T_1 relaxation time using a 3T MR imaging scanner. The T_1-weighted maps in Fig. 4(a) show that the T_1-weighted MR imaging signal intensity was continuously enhanced, resulting in brighter images with increasing mass. Furthermore, as shown in Fig. 4(b), the longitudinal proton relaxation rate as a function of PMMH nanoparticle concentration led to an r_1 relaxivity of 13.6 $mM^{-1}·s^{-1}$, which was much larger than that of Magnevist (r_1 = 4.5 $mM^{-1}·s^{-1}$) [35]. Additionally, ultrasound imaging experiments *in vitro* were performed. The results are shown in Figs. 4(c) and 4(d), which shows the ultrasound images of the dialysis bag (labeled in the blue frame) with H_2O and PMMH nanoparticles in the cross-section. As shown in Fig. 4(c), the weak signal was equal to that of the H_2O medium outside of the dialysis bag. However, PMMH nanoparticles showed relatively strong ultrasound signals in contrast to the H_2O medium outside of the dialysis bag because of the large differences in acoustic impedances between perfluorocarbons and water (Fig. 4(d)). In contrast, Fig. S5 in the ESM shows the MMH nanoparticles, which were slightly different. The results indicate that PMMH nanoparticles can be used for biomedical engineering in molecular imaging, including MR and ultrasound imaging.

Lymph ultrasound administration of the dual-mode contrast agent was performed *in vivo* in rabbit (Fig. 5). An attempt was made to locate lymph nodes in the knee popliteal fossa regions using primary gray scale sonography before PMMH nanoparticles were injected, which was helpful for observing the change in the lymph nodes after PMMH nanoparticle administration. After PMMH nanoparticle infusion, the increase in

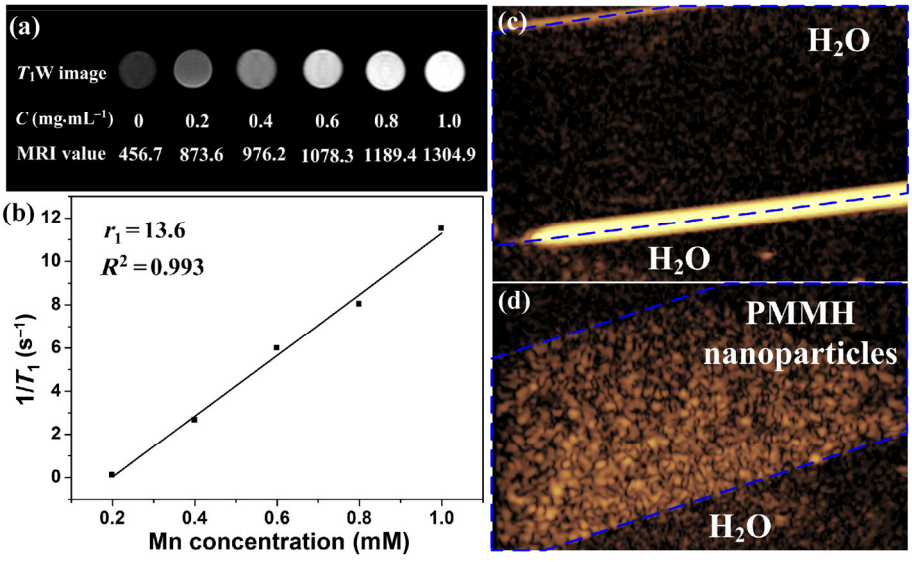

Figure 4 (a) T_1-weighted maps of various Mn concentrations *in vitro*, (b) the linear relationship between relaxation rates ($1/T_1$) and Mn concentrations and ultrasound images *in vitro* of (c) pure H_2O and (d) PMMH nanoparticles in a dialysis bag.

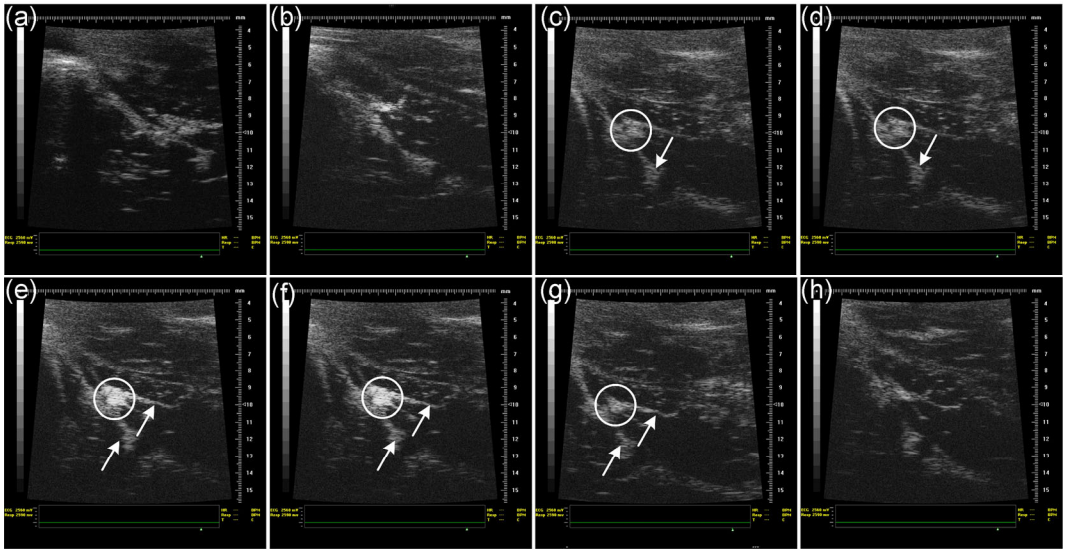

Figure 5 Ultrasound images *in vivo* of PMMH nanoparticles injection in rabbit knee popliteal fossa. Scanning time after hypodermic injection: (a) 0, (b) 5, (c) 15, (d) 25, (e) 35, (f) 45, (g) 55, and (h) 65 min.

lymph nodes signal intensity was observed gradually (labeled by circle). When the enhancement time was 15 min (Fig. 5(c)), the lymph node was imaged clearly. When the time was increased to 35 min, the lymph node was the brightest (Fig. 5(e)). Next, the signal decreased significantly at 55 and 65 min (Figs. 5(g) and 5(h)). Furthermore, closer observation revealed that lymph vessels around the lymph nodes were also imaged (labeled with an arrow). With increasing enhancement time, a larger number of lymph vessels gradually became clear. Maximum signals for the PMMH nanoparticles were reached at 35 min, followed by a decreased in the signals. These results show that the PMMH nanoparticles can be returned to the lymph nodes within 15 min through lymph vessels after hypodermic injection and retained for at least 30 min (from 15 to 45 min). Therefore, the PMMH nanoparticles may be used in ultrasound imaging *in vivo* with a slower metabolism, enabling more careful diagnosis without causing human body damage.

Furthermore, the MR imaging ability of the dual-mode contrast agent was evaluated. Based on the results of the ultrasound imaging, the injection site was chosen and the MR images were collected from 15 to 45 min. As shown in Fig. 6(a), the left lymph node (labeled with yellow arrow), imaged using commercial Gd-DTPA, clearly appeared within 15 min whereas the right lymph node (labeled with red arrow),

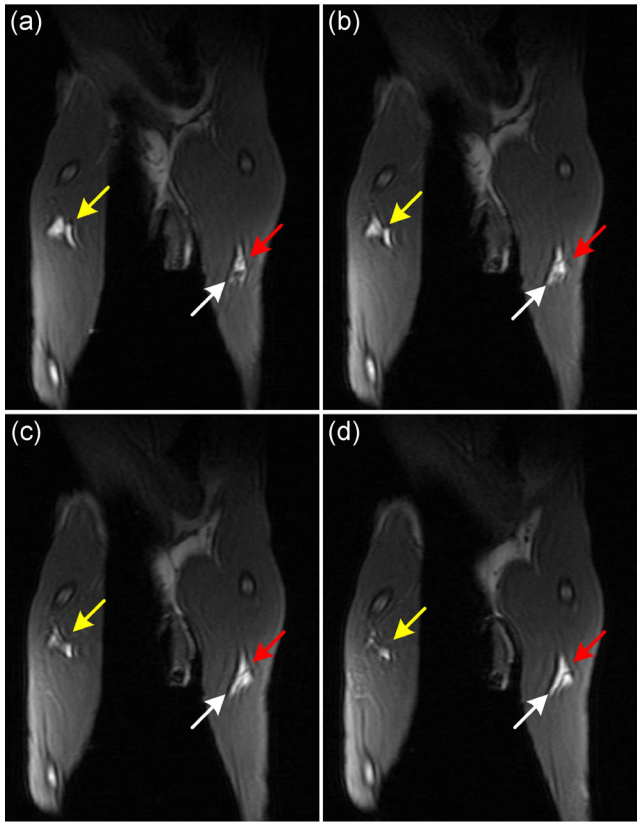

Figure 6 T_1-weighted MR images *in vivo* of commercial Gd-DTPA (left leg) and PMMH nanoparticles (right leg) injection in rabbit knee popliteal fossa. Scanning time after hypodermic injection: (a) 15, (b) 25, (c) 35, and (d) 45 min.

imaged using the PMMH nanoparticles, remained blurry. Closer observation revealed some vessels

around the lymph node in the right leg (labeled with white arrow). With increasing of enhancement time, the signal intensity of the left lymph node was weaker, while that of the right node was stronger (Figs. 6(b) and 6(c)). Additionally, these vessels were imaged gradually. With an enhancement time of 45 min, the lymph node of the left leg was almost not visible, suggesting that Gd-DPTA had begun to metabolize, but that of the right node remained clear, which was similar to the result of ultrasound imaging. These results illustrate that the enhancement caused by PMMH nanoparticles was higher than that of the commercial Gd-DPTA. Thus, the dual-mode contrast agent is useful for both ultrasound and MR imaging *in vivo*.

Immunofluorescence analysis of ultrasound or MR imaging tissue at 35 min post-injection of the PMMH nanoparticles was performed to demonstrate the ability of PMMH nanoparticles to penetrate into the lymph system. As shown in Fig. 7, the yellow cells, colocalized with the anti-human LYVE-1 polyclonal primary antibodies, revealed that the tissue abundantly expressed LYVE-1. Furthermore, the fluorescence image indicated that the zone encircled by yellow cells should be lymph vessels or lymph capillaries (labeled with white arrows). These results suggest that the imaged tissue expressed clear lymph characterization, where the PMMH nanoparticles penetrated through so as to enhance their imaging effect. Thus, the dual-mode contrast agent was shown to have good lymph system-targeted abilities *in vivo*.

Cytotoxicity was also investigated to examine the feasibility of the obtained PMMH nanoparticles for biomedical application. As shown in Fig. 8, the effect of different PMMH nanoparticles on cell proliferation was assessed in HCT116 cells using the CCK-8 assay. Using the viability of untreated cells as the control, the cellular viabilities decreased with increasing concentrations of PMMH nanoparticles, and approximately 80% cell viabilities were maintained even up to a relatively high dose of 125 $\mu g \cdot mL^{-1}$ after exposure for 12 h. Upon incubation with the PMMH nanoparticles at different concentrations, less than 20% of cells had died after 4, 8, and 12 h. Therefore, the results demonstrate that the obtained nanoparticles have low cytotoxicity.

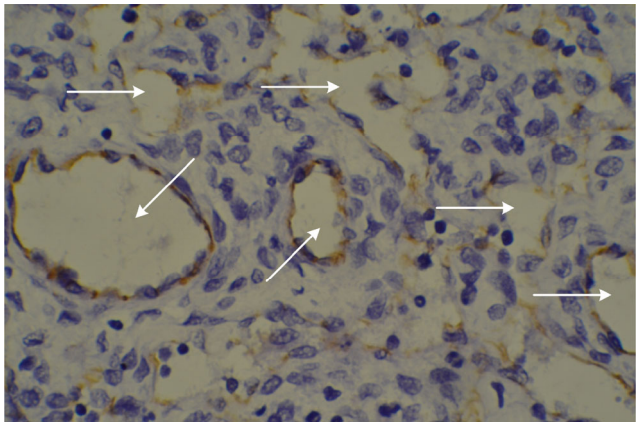

Figure 7 Immunohistochemical characterization of lymphatic markers.

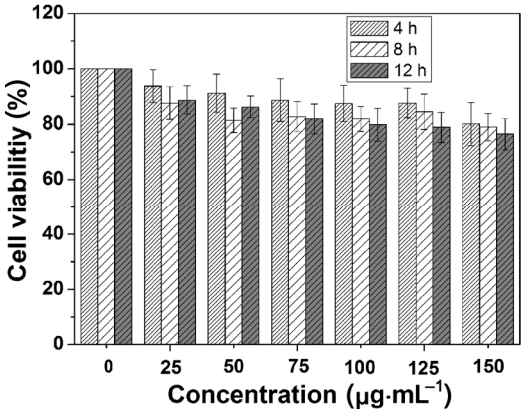

Figure 8 The CCK-8 assay results of the obtained PMMH nanoparticles.

In addition to the preparation of the PMMH nanoparticles for dual-mode imaging of the lymph system, the platform was also loaded with hydrophilic DOX to obtain DMMH nanoparticles for combined diagnose and therapy with MR imaging and sustained release for lymph tumors. As shown in Fig. 9(a), SEM imaging revealed that the DMMH nanoparticles were likely coated with organic nanoparticles compounds, with an average hydrodynamic size of 210 nm (Fig. S7 in the ESM). Compared to the TEM images of MMH nanoparticles (Fig. S6 in the ESM), the surface of DMMH nanoparticles were blurrier (Fig. 9(b)). The N_2 adsorption/desorption isotherm curve further confirmed that the surface area was 284 $m^2 \cdot g^{-1}$ (Fig. 9(c)) and the average pore size of DMMH nanoparticles was 2.6 nm (Fig. S8 in the ESM), indicating the more DOX absorption occurred in MMH nanoparticles than in PFOB. Furthermore, TEM image confirmed the

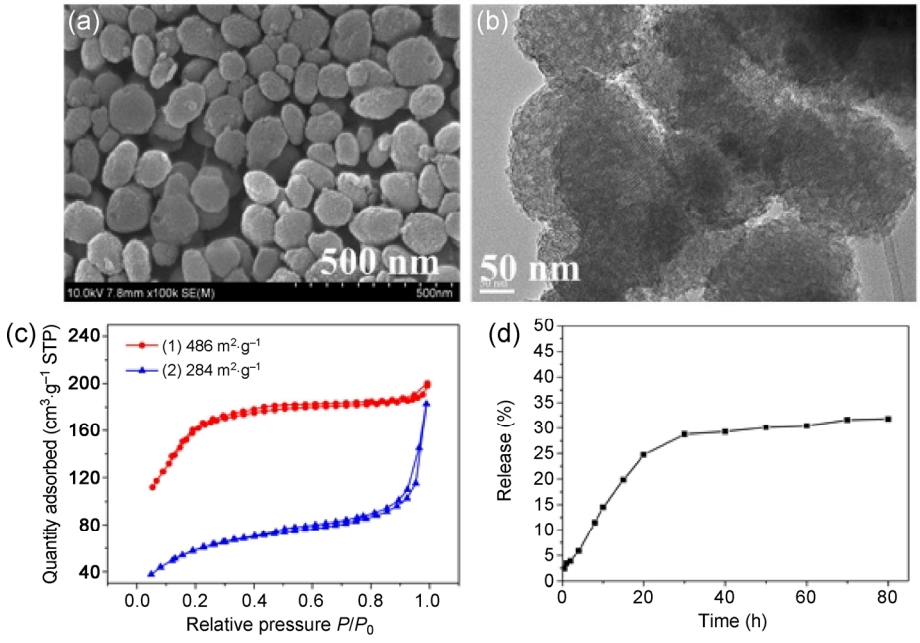

Figure 9 (a) SEM and (b) TEM of DMMH nanoparticles, (c) N_2 adsorption/desorption isotherm ((1): MMH nanoparticles and (2): DMMH nanoparticles)) and (d) DOX release curve from DMMH nanoparticles.

above speculation. DOX loading in MMH nanoparticles was determined to be as high as 43.7 mg·g^{-1}. The loading amount was much lower than that of reported manganese oxide/MSNs composite (382 mg·g^{-1}), but was similar to that of ZnO quantum dots modified with mesoporous silica (40 mg·g^{-1}) [36]. The difference may be that the mesoporous channels were pre-filled with HA molecules, increasing the difficulty of DOX absorption. The loading content was much higher than that of PFOB in MMH nanoparticles, which may have resulted from the driving force among the hydrophilic and hydrophobic molecules penetrating into our mesoporous silica. As shown in Fig. 2, the driving force of the hydrophobic PFOB molecule in MMH nanoparticles may have resulted in a hydrophobic interaction between PFOB and HA molecules around HA in mesoporous pores. However, similar to the results of a previous study, the driving force of the hydrophilic DOX molecule in MMH nanoparticles were the molecular interactions between DOX and HA molecules around HA molecule inside and/or outside the mesoporous pores, such as hydrogen bonds and Van der Waals forces [37, 38]. The results were in accordance with the decrease in the specific surface area, from 486 m^2·g^{-1} of the MMH nanoparticles to 374 m^2·g^{-1} of PMMH nanoparticles and to 284 m^2·g^{-1} of DMMH nanoparticles (Fig. 9(c)). Furthermore, we investigated the drug loading and release behavior of the DMMH nanoparticles. The UV–vis absorption spectra of DOX at 0.1 mg·mL^{-1} of the DMMH nanoparticles are shown in Fig. S9 (in the ESM). The absorption spectra of DOX in DMMH showed characteristic absorption peaks at 490 nm, which were similar to those reported in the literature [10, 39–42]. Figure 9(d) further shows the release behavior of DOX from the DMMH nanoparticles in PBS (pH 5.5), which is related to the acidic tumor environment. The final release was observed to be 31.8% at 80 h (Fig. 9(d)) and 49.1% on the 10th day (Fig. S10 in the ESM), demonstrating that the DOX inside the channels of DMMH could be released slowly. The drug release curve showed sustained release behavior and the drug was progressively released by desorption and diffusion to the PBS solution. These results indicate that the DMMH nanoparticles have favorable DOX release properties.

To examine the feasibility of the obtained DMMH nanoparticles for *in vitro* growth inhibition on tumor cells, their cell cytotoxicity and uptake on HCT116 cells were investigated. As shown in Fig. 10(a), growth inhibition of the cells was observed after incubation with free DOX and DMMH nanoparticles. These results

indicate the dose-dependent cytotoxicity behavior, revealing that the DMMH nanoparticles had remarkably higher anticancer efficiency than that of free DOX. Furthermore, the IC_{50} values are 7.9 μg·mL^{-1} DOX in the DMMH nanoparticles and 10.6 μg·mL^{-1} free DOX also indicated that DMMH nanoparticles increased the *in vitro* growth inhibitory effect. The enhancement of anticancer efficiency may have resulted from the high combining ability of HA and CD44, possibly enhancing their antitumor effects. Because of the excellent MR imaging *in vitro* and *in vivo* and targeting specificity of the universal platform, we further explored the potential of using the DMMH nanoparticles for diagnosis and treatment of a xenografted tumor model. As shown in Fig. 11(a), the tumor-bearing nude mice with tumor volumes of approximately 123.5 mm^3 were intratumorally injected with 0.2 mL 0.10 mg·mL^{-1} DMMH nanoparticles. Before and after 5 and 10 min post-injection, the nude mice were imaged by MR (Fig. 11(a)). Compared to before injection, the single of tumor region clearly increased in a typical T_1-weighted MR image at 5 and 10 min after injection.

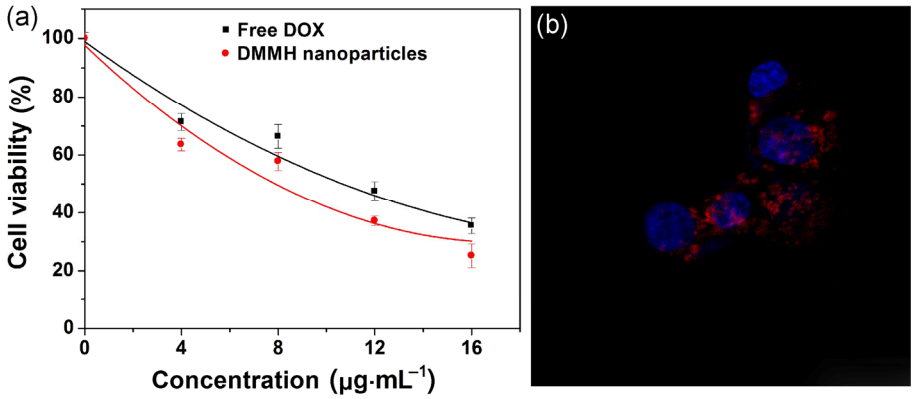

Figure 10 (a) Inhibitory effect of DMMH nanoparticles and free DOX on HCT116 cells as examined by CCK-8 assay and (b) laser scanning confocal microscopy images of HCT116 cells incubated with DMMH nanoparticles.

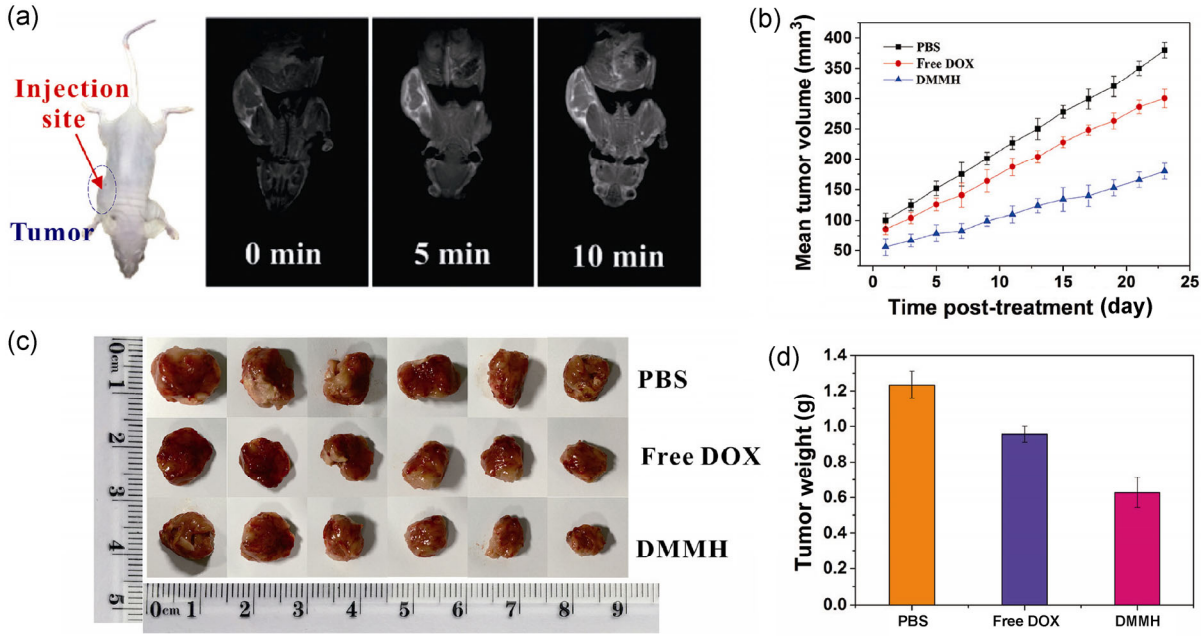

Figure 11 (a) Photograph of the tumor-bearing nude mice for MR imaging and MR images at different scanning time, (b) Mean tumor volume of the mice in different groups after treatment, (c) photograph of the tumors from different groups after treatment and (d) mean body weights of the mice in different groups after treatment. Data represent the mean ± standard deviation of seven mice. $P < 0.05$ was considered to be statistically significant difference and shown by asterisks.

Closer observation revealed subtle structures in the tumor region. These results suggest that intratumoral injection of the DMMH nanoparticles lead to the uniform distribution of the particles within the tumor region, allowing for effective MR imaging of the whole tumor and showing that the obtained DMMH nanoparticles have great potential to be used as a contrast agent for *in vivo* tumor MR imaging.

To investigate the therapeutic efficacy of the DMMH nanoparticles *in vivo*, comparative studies of the effectiveness of tumor inhibition were conducted. Eighteen tumor-bearing nude mice were randomly distributed into three groups, including the PBS, free DOX, and DMMH nanoparticles groups, which were administered the same dosage of free DOX. After two weeks of feeding, the three groups of nude mice were intratumorally injected with DMMH nanoparticles (0.2 mL, 0.1 mg·mL^{-1}), free DOX, and PBS (0.2 mL), respectively. No mice died and their volume was measured during the course of therapy. As shown in Fig. 11(b), the mean tumor volume of the DMMH nanoparticle group increases most rapidly among the three groups, indicating that the DMMH nanoparticles have considerable growth inhibitory effect on tumors. Furthermore, on day 23, the mice were sacrificed and tumors were excised and weighed. The tumor photograph and mean tumor weights in each group after treatment are shown in Figs. 11(c) and 11(d). The DMMH nanoparticles group also showed enhanced inhibition activity compared to the PBS and free DOX groups. The mean tumor weight in the DMMH nanoparticles group (0.618 ± 0.137 g) was smaller than that of the PBS group (1.270 ± 0.109 g) and free DOX group (0.978 ± 0.098 g, $P < 0.05$). The results indicate that treatment with the DMMH nanoparticles significantly enhanced antitumor activity over the long-term, which was attributed to DOX chemotherapy released from DMMH nanoparticles [10, 40, 41, 43, 44]. The above results reveal that the DMMH nanoparticles are a powerful agent for the combined diagnosis and therapy of cancer *in vivo*.

The short-term and long-term distribution of the universal platform (MMH nanoparticles) in mice was determined to evaluate their safety. As shown in Fig. 12(a) of the single injection of MMH nanoparticles, Mn could be detected in all organs besides the blood, but not detected in any organ in the control group, where the maximum concentration was found in the liver. Furthermore, the concentration-time curves revealed a rapid decline in Mn concentration for 12 h after injection. At 12 h, a high Mn concentration was observed in the liver, spleen, and kidneys, while organs besides the blood were at lower levels. The results showed that MMH nanoparticles were distributed mainly to the liver, followed by the spleen and kidneys. Furthermore, repeated administration resulted in accumulation in the liver, spleen, and kidneys, indicating that these organs target organs for the excretion of MMH nanoparticles [45]. The above results indicate that the MMH nanoparticles distribute in most of internal organs through blood flow and were finally metabolized in the liver, spleen, and kidneys.

4 Conclusions

In summary, a new universal platform of MM nanoparticles with MR imaging was designed by doping Mn^{2+} into the framework of mesoporous silica. HA-

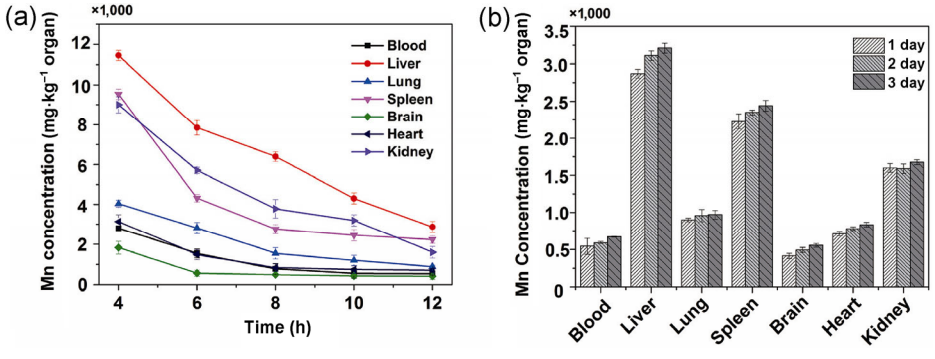

Figure 12 Mean Mn concentrations (mg/kg) per gram organ over time after one single injection (a) and consecutive injection (b), error bars represent standard deviations.

modified MM nanoparticles can be used for *in vitro* and *in vivo* targeting of the lymph system to produce MMH nanoparticles. Two standard compounds, hydrophobic PFOB and hydrophilic DOX, were loaded into channels to obtain PMMH or DMMH nanoparticles for dual-mode imaging and imaging and therapy, respectively. We demonstrated that the PMMH and DMMH nanoparticles were highly targeted to the lymph system *in vitro* and *in vivo*, and the MR/ultrasound imaging of PMMH nanoparticles in the lymph system, and MR imaging and therapeutic ability of DMMH nanoparticles in cancer is highlighted. Furthermore, nanoparticles were distributed and excreted mainly in the liver followed by the spleen and kidneys. The Mn@mSiO_2-based nanoparticles are promising for many applications in biomedicine, including multimodality imaging, cell tracking, and cancer therapies. Our results provide a new universal platform that can be used in further studies and has great potential for use in biological applications.

Acknowledgements

The work is supported by Shanghai Rising-Star Program (No. 13QB1402200), Shanghai Minhang district talent development special fund, National Key Technology Research and Development Program (No. 2014BAK05B02) and National Natural Science Foundation of China (Nos. 81271638 and 81371622).

Electronic Supplementary Material: Supplementary material is available in the online version of this article at http://dx.doi.org/10.1007/s12274-015-0929-1.

References

[1] Jin, Y. D.; Gao, X. H. Plasmonic fluorescent quantum dots. *Nat. Nanotechnol.* **2009**, *4*, 571–576.

[2] Hu, S. H.; Gao, X. H. Nanocomposites with spatially separated functionalities for combined imaging and magnetolytic therapy. *J. Am. Chem. Soc.* **2010**, *132*, 7234–7237.

[3] Fan, W. P.; Shen, B.; Bu, W. B.; Chen, F.; Zhao, K. L.; Zhang, S. J.; Zhou, L. P.; Peng, W. J.; Xiao, Q. F.; Xing, H. Y. et al. Rattle-structured multifunctional nanotheranostics for synergetic chemo-/radiotherapy and simultaneous magnetic/luminescent dual-mode imaging. *J. Am. Chem. Soc.* **2013**, *135*, 6494–6503.

[4] Passuello, T.; Pedroni, M.; Piccinelli, F.; Polizzi, S.; Marzola, P.; Tambalo, S.; Conti, G.; Benati, D.; Vetrone, F.; Bettinelli, M. et al. PEG-capped, lanthanide doped GdF_3 nanoparticles: Luminescent and T_2 contrast agents for optical and MRI multimodal imaging. *Nanoscale* **2012**, *4*, 7682–7689.

[5] Pellegatti, L.; Zhang, J.; Drahos, B.; Villette, S.; Suzenet, F.; Guillaumet, G.; Petoud, S.; Tóth, E. Pyridine-based lanthanide complexes: Towards bimodal agents operating as near infrared luminescent and MRI reporters. *Chem. Commun.* **2008**, 6591–6593.

[6] Nishioka, T.; Shiga, T.; Shirato, H.; Tsukamoto, E.; Tsuchiya, K.; Kato, T.; Ohmori, K.; Yamazaki, A.; Aoyama, H.; Hashimoto, S. et al. Image fusion between ^{18}FDG-PET and MRI/CT for radiotherapy planning of oropharyngeal and nasopharyngeal carcinomas. *Int. J. Radiat. Oncol.* **2002**, *53*, 1051–1057.

[7] Wen, S. H.; Li, K. G.; Cai, H. D.; Chen, Q.; Shen, M. W.; Huang, Y. P.; Peng, C.; Hou, W. X.; Zhu, M. F.; Zhang, G. X. et al. Multifunctional dendrimer-entrapped gold nanoparticles for dual mode CT/MR imaging applications. *Biomaterials* **2013**, *34*, 1570–1580.

[8] Kubota, K.; Yokoyama, J.; Yamaguchi, K.; Ono, S.; Qureshy, A.; Itoh, M.; Fukuda, H. FDG-PET delayed imaging for the detection of head and neck cancer recurrence after radiochemotherapy: Comparison with MRI/CT. *Eur. J. Nucl. Med. Mol. Imag.* **2004**, *31*, 590–595.

[9] Cheng, S. H.; Lee, C. H.; Chen, M. C.; Souris, J. S.; Tseng, F. G.; Yang, C. S.; Mou, C. Y.; Chen, C. T.; Lo, L. W. Trifunctionalization of mesoporous silica nanoparticles for comprehensive cancer theranostics-the trio of imaging, targeting and therapy. *J. Mater. Chem.* **2010**, *20*, 6149–6157.

[10] Cho, H. J.; Yoon, H. Y.; Koo, H.; Ko, S. H.; Shim, J. S.; Cho, J. H.; Park, J. H.; Kim, K.; Kwon, I. C.; Kim, D. D. Hyaluronic acid-ceramide-based optical/MR dual imaging nanoprobe for cancer diagnosis. *J. Controlled Release* **2012**, *162*, 111–118.

[11] Yang, K.; Hu, L. L.; Ma, X. X.; Ye, S. Q.; Cheng, L.; Shi, X. Z.; Li, C. H.; Li, Y. G.; Liu, Z. Multimodal imaging guided photothermal therapy using functionalized graphene nanosheets anchored with magnetic nanoparticles. *Adv. Mater.* **2012**, *24*, 1868–1872.

[12] Zha, Z. B.; Wang, J. R.; Zhang, S. H.; Wang, S. M.; Qu, E. Z.; Zhang, Y. Y.; Dai, Z. F. Engineering of perfluorooctylbromide polypyrrole nano-/microcapsules for simultaneous contrast enhanced ultrasound imaging and photothermal treatment of cancer. *Biomaterials* **2014**, *35*, 287–293.

[13] Bhang, S. H.; Won, N.; Lee, T. J.; Jin, H.; Nam, J.; Park, J.; Chung, H.; Park, H. S.; Sung, Y. E.; Hahn, S. K. et al. Hyaluronic acid-quantum dot conjugates for *in vivo* lymphatic vessel imaging. *Acs Nano* **2009**, *3*, 1389–1398.

[14] Jaggupilli, A.; Elkord, E. Significance of CD44 and CD24 as cancer stem cell markers: An enduring ambiguity. *Clin. Dev. Immunol.* **2012**, *2012*, 708036.

[15] Kim, J. H.; Glant, T. T.; Lesley, J.; Hyman, R.; Mikecz, K. Adhesion of lymphoid cells to CD44-specific substrata: The consequences of attachment depend on the ligand. *Exp. Cell Res.* **2000**, *256*, 445–453.

[16] Banerji, S.; Ni, J.; Wang, S. X.; Clasper, S.; Su, J.; Tammi, R.; Jones, M.; Jackson, D. G. LYVE-1, a new homologue of the CD44 glycoprotein, is a lymph-specific receptor for hyaluronan. *J. Cell Biol.* **1999**, *144*, 789–801.

[17] Jackson, D. G.; Prevo, R.; Clasper, S.; Banerji, S. LYVE-1, the lymphatic system and tumor lymphangiogenesis. *Trends Immunol.* **2001**, *22*, 317–321.

[18] Mizrahy, S.; Raz, S. R.; Hasgaard, M.; Liu, H.; Soffer-Tsur, N.; Cohen, K.; Dvash, R.; Landsman-Milo, D.; Bremer, M. G. E. G.; Moghimi, S. M. et al. Hyaluronan-coated nanoparticles: The influence of the molecular weight on CD44-hyaluronan interactions and on the immune response. *J. Controlled Release* **2011**, *156*, 231–238.

[19] Wu, G. Y.; Zhang, H. J.; Zhan, Z. F.; Lu, Q.; Cheng, J. J.; Xu, J. R.; Zhu, J. Hyaluronic acid-gadolinium complex nanospheres as lymphatic system-specific contrast agent for magnetic resonance imaging. *Chinese J. Chem.* **2015**, *33*, 1153–1158.

[20] Ma, M.; Xu, H. X.; Chen, H. R.; Jia, X. Q.; Zhang, K.; Wang, Q.; Zheng, S. G.; Wu, R.; Yao, M. H.; Cai, X. J. et al. A drug-perfluorocarbon nanoemulsion with an ultrathin silica coating for the synergistic effect of chemotherapy and ablation by high-intensity focused ultrasound. *Adv. Mater.* **2014**, *26*, 7378–7385.

[21] Choi, K. Y.; Yoon, H. Y.; Kim, J. H.; Bae, S. M.; Park, R. W.; Kang, Y. M.; Kim, I. S.; Kwon, I. C.; Choi, K.; Jeong, S. Y. et al. Smart nanocarrier based on PEGylated hyaluronic acid for cancer therapy. *Acs Nano* **2011**, *5*, 8591–8599.

[22] Choi, K. Y.; Min, K. H.; Yoon, H. Y.; Kim, K.; Park, J. H.; Kwon, I. C.; Choi, K.; Jeong, S. Y. PEGylation of hyaluronic acid nanoparticles improves tumor targetability *in vivo*. *Biomaterials* **2011**, *32*, 1880–1889.

[23] Park, S. J.; Park, W.; Na, K. Photo-activatable ternary complex based on a multifunctional shielding material for targeted shRNA delivery in cancer treatment. *Biomaterials* **2013**, *34*, 8991–8999.

[24] He, Q. J.; Shi, J. L. Mesoporous silica nanoparticle based nano drug delivery systems: Synthesis, controlled drug release and delivery, pharmacokinetics and biocompatibility. *J. Mater. Chem.* **2011**, *21*, 5845–5855.

[25] Sim, L. N.; Majid, S. R.; Arof, A. K. FTIR studies of PEMA/PVdF-HFP blend polymer electrolyte system incorporated with $LiCF_3SO_3$ salt. *Vib. Spectrosc.* **2012**, *58*, 57–66.

[26] Sim, L. N.; Majid, S. R.; Arof, A. K. Effects of 1-butyl-3-methyl imidazolium trifluoromethanesulfonate ionic liquid in poly(ethyl methacrylate)/poly(vinylidenefluoride-co-hexafluoropropylene) blend based polymer electrolyte system. *Electrochim. Acta* **2014**, *123*, 190–197.

[27] Guillet-Nicolas, R.; Laprise-Pelletier, M.; Nair, M. M.; Chevallier, P.; Lagueux, J.; Gossuin, Y.; Laurent, S.; Kleitz, F.; Fortin, M. A. Manganese-impregnated mesoporous silica nanoparticles for signal enhancement in MRI cell labelling studies. *Nanoscale* **2013**, *5*, 11499–11511.

[28] Bejar, A.; Ben Chaabene, S.; Jaber, M.; Lambert, J. F.; Bergaoui, L. Mn-analcime: Synthesis, characterization and application to cyclohexene oxidation. *Micropor. Mesopor. Mat.* **2014**, *196*, 158–164.

[29] Liu, Y.; Shen, J. M.; Chen, Z. L.; Liu, Y. Degradation of p-chloronitrobenzene in drinking water by manganese silicate catalyzed ozonation. *Desalination* **2011**, *279*, 219–224.

[30] Päll, T.; Pink, A.; Kasak, L.; Turkina, M.; Anderson, W.; Valkna, A.; Kogerman, P. Soluble CD44 interacts with intermediate filament protein vimentin on endothelial cell surface. *PLoS One* **2011**, *6*, e29305.

[31] Jones, M.; Tussey, L.; Athanasou, N.; Jackson, D. G. Heparan sulfate proteoglycan isoforms of the CD44 hyaluronan receptor induced in human inflammatory macrophages can function as paracrine regulators of fibroblast growth factor action. *J. Biol. Chem.* **2000**, *275*, 7964–7974.

[32] Appaturi, J. N.; Adam, F. A facile and efficient synthesis of styrene carbonate via cycloaddition of CO_2 to styrene oxide over ordered mesoporous MCM-41-Imi/Br catalyst. *Appl. Catal. B-Environ.* **2013**, *136–137*, 150–159.

[33] Banerji, S.; Hide, B. R. S.; James, J. R.; Noble, M. E. M.; Jackson, D. G. Distinctive properties of the hyaluronan-binding domain in the lymphatic endothelial receptor lyve-1 and their implications for receptor function. *J. Biol. Chem.* **2010**, *285*, 10724–10735.

[34] Faul, C.; Donnelly, M.; Merscher-Gomez, S.; Chang, Y. H.; Franz, S.; Delfgaauw, J.; Chang, J. M.; Choi, H. Y.; Campbell, K. N.; Kim, K. et al. The actin cytoskeleton of kidney podocytes is a direct target of the antiproteinuric effect of cyclosporine A. *Nat. Med.* **2008**, *14*, 931–938.

[35] Stanisz, G. J.; Henkelman, R. M. Gd-DTPA relaxivity depends on macromolecular content. *Magn. Reson. Med.* **2000**, *44*, 665–667.

[36] Muharnmad, F.; Guo, M. Y.; Qi, W. X.; Sun, F. X.; Wang, A. F.; Guo, Y. J.; Zhu, G. S. pH-triggered controlled drug release from mesoporous silica nanoparticles via intracelluar dissolution of ZnO nanolids. *J. Am. Chem. Soc.* **2011**, *133*, 8778–8781.

[37] Zhao, W. W.; Cui, B.; Peng, H. X.; Qiu, H. J.; Wang, Y. Y. Novel method to investigate the interaction force between etoposide and APTES-functionalized Fe_3O_4@nSiO_2@mSiO_2 nanocarrier for drug loading and release processes. *J. Phys. Chem. C* **2015**, *119*, 4379–4386.

[38] Mathew, A.; Parambadath, S.; Park, S. S.; Ha, C. S. Hydrophobically modified spherical MCM-41 as nanovalve system for controlled drug delivery. *Micropor. Mesopor. Mat.* **2014**, *200*, 124–131.

[39] de la Torre, C.; Casanova, I.; Acosta, G.; Coll, C.; Moreno, M. J.; Albericio, F.; Aznar, E.; Mangues, R.; Royo, M.; Sancenon, F. et al. Gated mesoporous silica nanoparticles using a double-role circular peptide for the controlled and target-preferential release of doxorubicin in CXCR4-expresing lymphoma cells. *Adv. Funct. Mater.* **2015**, *25*, 687–695.

[40] Niu, C. C.; Wang, Z. G.; Lu, G. M.; Krupka, T. M.; Sun, Y.; You, Y. F.; Song, W. X.; Ran, H. T.; Li, P.; Zheng, Y. Y. Doxorubicin loaded superparamagnetic PLGA-iron oxide multifunctional microbubbles for dual-mode US/MR imaging and therapy of metastasis in lymph nodes. *Biomaterials* **2013**, *34*, 2307–2317.

[41] Yang, X. Y.; Wang, Y. S.; Huang, X.; Ma, Y. F.; Huang, Y.; Yang, R. C.; Duan, H. Q.; Chen, Y. S. Multi-functionalized graphene oxide based anticancer drug-carrier with dual-targeting function and pH-sensitivity. *J. Mater. Chem.* **2011**, *21*, 3448–3454.

[42] Chen, Z. W.; Li, Z. H.; Lin, Y. H.; Yin, M. L.; Ren, J. S.; Qu, X. G. Biomineralization inspired surface engineering of nanocarriers for pH-responsive, targeted drug delivery. *Biomaterials* **2013**, *34*, 1364–1371.

[43] Sun, J. S.; Xianyu, Y. L.; Li, M. M.; Liu, W. W.; Zhang, L.; Liu, D. B.; Liu, C.; Hu, G. Q.; Jiang, X. Y. A microfluidic origami chip for synthesis of functionalized polymeric nanoparticles. *Nanoscale* **2013**, *5*, 5262–5265.

[44] Yu, L. L.; Bi, H. Facile synthesis and magnetic property of iron oxide/MCM-41 mesoporous silica nanospheres for targeted drug delivery. *J. Appl. Phys.* **2012**, *111*, 07B514.

[45] Lankveld, D. P. K.; Oomen, A. G.; Krystek, P.; Neigh, A.; Troost-de Jong, A.; Noorlander, C. W.; Van Eijkeren, J. C. H.; Geertsma, R. E.; De Jong, W. H. The kinetics of the tissue distribution of silver nanoparticles of different sizes. *Biomaterials* **2010**, *31*, 8350–8361.